Journal of Multimedia Techniques (2020) Vol. 1: 1-12
Clausius Scientific Press, Canada
DOI: 10.23977/jmult.2020.010101
ISSN 2516-4716

Research on vignetting correction method of thermal infrared remote sensing image assisted by high resolution data

Hang Chen,[1,3] Camel Tanougast,[2] Walter Blondel[3] and Feifei Liu[1*]

[1] *School of Electrical Engineering and Automation, Jiangxi University of Science and Technology, Ganzhou, 341000, China*

[2]*Laboratoire Conception Optimisation et Modélisation des Systèms, University de Lorraine, Metz 57070, France*

[3] *Université de Lorraine, CNRS, CRAN UMR 7039, Nancy 54000, France*

Keywords: Thermal infrared image; Geometric correction; Simulation image; Scale invariant feature transformation

Abstract: With the continuous development of thermal infrared remote sensing technology, thermal infrared remote sensing image is widely used in land surface temperature inversion, forest fire monitoring, mineral detection and so on. In these applications, geometric correction of thermal infrared image is an important basic technology. Taking advantage of the high spatial resolution of gf-2 satellite, a method combining simulated image and feature matching is proposed by analyzing the imaging difference and correlation of heterogeneous loads. This method is based on high-resolution optical image, and based on the ground radiation basic data, first of all, from the perspective of thermal infrared radiation, the transition image is formed, which is used to assist the geometric correction of thermal infrared image; then, the scale invariant feature transformation operator is used to detect the feature points, so as to obtain the same points and improve the geometric correction accuracy of thermal infrared image.

1. Introduction

With the continuous advancement of China's high-resolution earth observation program, the application of multi-source remote sensing images is gradually deepening. It is of great significance to make full use of the advantages of multi-source data to improve the accuracy of thermal infrared image geometric correction. The registration of high spatial resolution visible image and thermal infrared image is an important part [1-2]. The registration of visible image and infrared image belongs to heterogeneous image registration. The common matching methods of heterogeneous image include mutual information based matching and feature-based matching. Throughout the current research, most matching methods mainly focus on image features, but less

use of radiation information containing important information of heterogeneous images [3]. The infrared image reflects the radiation information of the ground object, while the visible light image reflects the reflection information of the ground object. The physical meaning of the two kinds of information is not the same. At the same time, the different imaging conditions of the sensor and the complexity of the ground object also cause the difference of the gray characteristics between the two images. Therefore, the lack of high-precision consistency between the two methods makes the registration difficult. Based on the advantages of existing high-resolution satellite images and focusing on the radiation information mechanism of ground objects, a method combining simulation image with feature matching is proposed to realize geometric correction of thermal infrared images.

2 Thermal infrared image geometric correction method based on image simulation

In this paper, the following strategies are adopted to realize the geometric correction of thermal infrared image assisted by high-resolution optical satellite image: firstly, based on the optical satellite image processed by geometric precision correction, combined with the specific emissivity data of typical ground objects and temperature statistical information, the image simulation is carried out from the perspective of thermal infrared radiation, and a transition image with similar hue characteristics as the thermal infrared image is formed[4] . Then, feature extraction operator is used to extract feature points from simulated image and thermal infrared image respectively, and a series of feature point pairs are obtained, and all mismatching points are screened out to obtain corresponding homonymous point pairs [5-6]. Finally, the coefficients of the geometric correction formula are calculated by using the selected control points of the same name to realize the geometric correction of thermal infrared images.

The specific process is shown in the following figure 1.

The main goal of this paper is to mine the representative action segment C from the infrared remote sensing image P. each action segment C can be regarded as a local linear piece (locally with Euclidean property). Generally speaking, the local linearity is determined by the ratio of geodesic distance to Euclidean distance between point pairs in the segment

$$\beta = \frac{1}{|C|^2} \sum_{i \in C} \sum_{j \in C} R\left(p_{(i)}, p_{(j)}\right) \quad (1)$$

Among them, C is the number of human postures contained in motion segment C, and B $R\left(p_{(i)}, p_{(j)}\right)$ is the ratio of geodesic distance to Euclidean distance between pose points $p_{(i)}$ and $p_{(j)}$:

$$R\left(p_{(i)}, p_{(j)}\right) = D_G\left(p_{(i)}, p_{(j)}\right) / D_E\left(p_{(i)}, p_{(j)}\right) \quad (2)$$

Euclidean distance $D_E\left(p_{(i)}, p_{(j)}\right)$ is LZ norm, while geodesic distance $D_G\left(p_{(i)}, p_{(j)}\right)$ is calculated by Dijkstra algorithm based on the established k-nearest neighbor graph. The schematic diagram of characteristic distance between image sequence frames is shown in Figure

2.

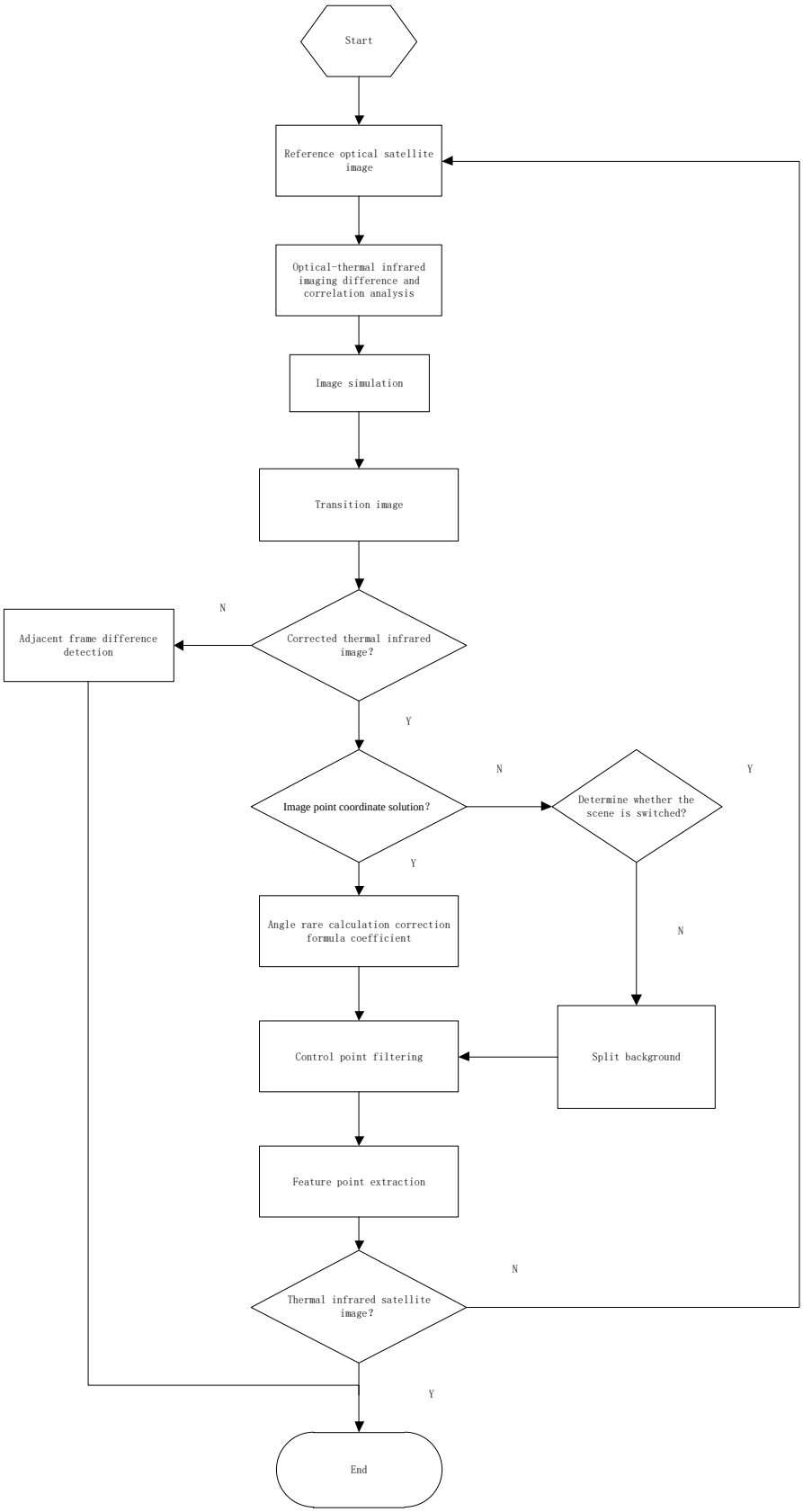

Fig. 1 Flow chart of thermal infrared image geometric correction based on image simulation

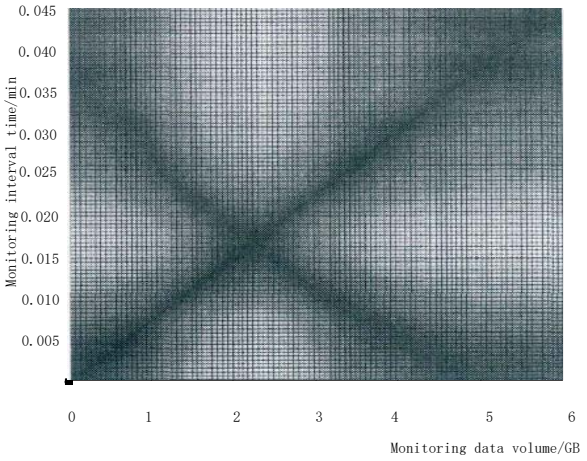

Fig. 2 Schematic diagram of feature distance between sequence frames

The method of constructing connected graph can well describe the feature relationship between unordered images, and has a strong application in the field of image set based recognition. However, the temporal relationship is very important for action recognition. The construction of the connected graph ignores the timing, which makes it not suitable for mining local segments in the action manifold [7].

As shown in Figure 2, the abscissa and ordinate are the frame ordinals respectively, and the color of corresponding points represents the feature distance between the two frames.

In order to describe the temporal relationship between fragments, a segmentation algorithm based on manifold local linearity measure is used to segment. A human action pose sequence $P=\left\{P_{(1)},P_{(2)},\ldots,P_{(F)}\right\}$ can be regarded as a manifold composed of a series of ordered pose points embedded in high-dimensional space, and the manifold is divided into two balanced linear subsequences. The division method is shown in Figure 3:

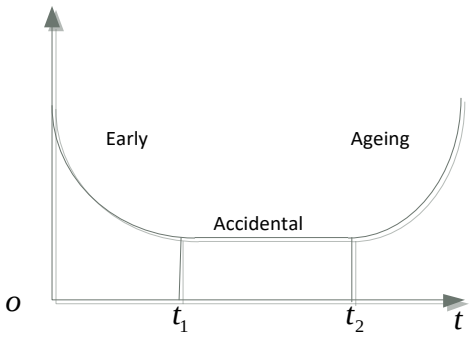

Fig. 3 Division mode

The subsequences are expressed as follows:

$$P_L=\left\{P_{(1)},P_{(2)},\ldots,P_{(d)}\right\} \quad (3)$$

$$P_R=\left\{P_{(d+1)},P_{(d+2)},\ldots,P_{(F)}\right\} \quad (4)$$

The division is as follows:

$$\beta_{L/R} = \frac{1}{\left|P_{L/R}\right|^2} \sum_{i \in P_{L/R}} \sum_{j \in P_{L/R}} R\left(p_{(i)}, p_{(j)}\right) \quad (5)$$

Among them, $P_{L/R}$ represents the left subsequence action fragment or the right subsequence action fragment, and the other symbols represent the information that can be analogized with formula (4). The local linearity measure combines the feature distance information of, so it has robust measurement and comprehensive representation for local linearity.

In each extension step, only the correlation distance between each human posture in the current left or right subsequence is calculated: Euclidean distance, geodesic distance and distance ratio. Therefore, the implementation of this expansion step is very efficient [8-9].

On the other hand, the k-order adjacency graph defined in this paper avoids the high time complexity of Dijkstra algorithm in the calculation of geodesic distance, so the calculation of local linearity measurement $\beta_{\mathrm{L/R}}$ can be carried out efficiently. In addition, when $\beta_{\mathrm{L}} = \beta_{\mathrm{R}}$ is used, it tends to divide the original sequence more balanced under the condition of local linearity measurement [10].

Positive potential is an ERP feature, which is related to the visual stimulus received by the subjects. Variance processing analysis of LPP segment data shows that the late positive time domain resolution is more than 60%. Based on the late positive potential criterion, the x-sequence signal (beta wave) and Y-sequence signal (θ wave) within 1000-1500ms after each picture stimulation were selected to calculate the wave frequency and average power to the band in this time period. The average power calculation formula of θ wave is shown in formula (6):

$$W_{\theta} = \sum_{i=1000}^{1500} Y_i^2 \quad (6)$$

The average power calculation formula of β wave is shown in formula (7):

$$W_{\beta} = \sum_{i=1000}^{1500} X_i^2 \quad (7)$$

The Sasi values of positive potential in the later period were calculated, and the differences between the power of θ wave and β wave were compared. Sasi can be used to detect visual signals in a balanced state, and wave frequency is used to characterize the power difference between theta wave and beta wave.

The calculation formula of asymmetry index of resting electric signal is as follows:

$$SASI = \frac{W_{\beta} - W_{\theta}}{W_{\beta} + W_{\theta}} \quad (8)$$

The above formula shows that the power of θ wave and β wave will change with different emotional state. The extracted electrical signal is calculated by wavelet transform, and the high

frequency interference is filtered out, and the time sequence signals X and y are obtained.

3 Geometric correction experiment of thermal infrared image based on image simulation

3.1 Experimental design

The infrared image is shown in the infrared image.

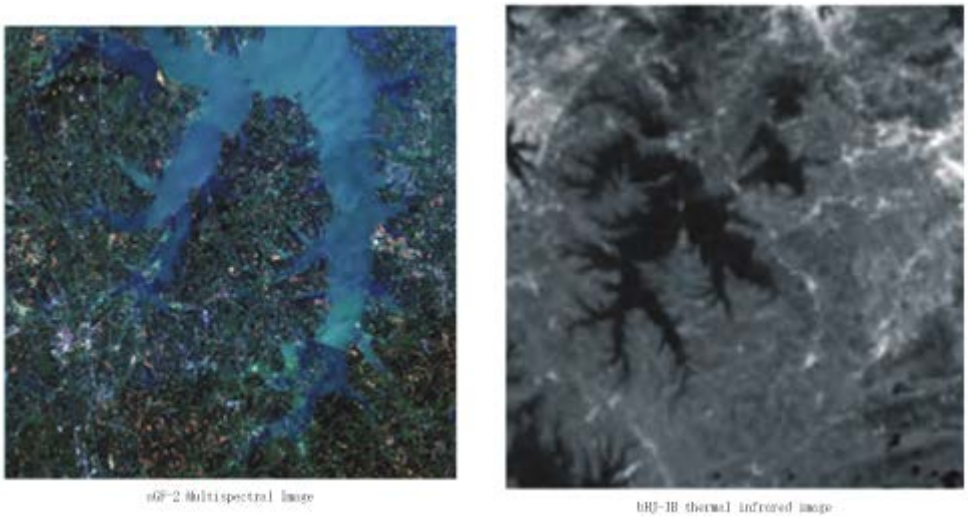

Fig. 4 Experimental images

Among them, the uf-2 image is the reference image, and the ground resolution is 4m,it includes visible light and near-infrared band, the blue band spectrum range is 0.45-v0.52 μ M, the spectral range of green band is 0.52-0.59 μ M, the red band spectrum range is 0.63-0.69 μ M,HJ-1B,The spectral range of the near-infrared band is 0.77-v0.89 μ M; The thermal infrared image is to be corrected ,the spatial resolution is 300 m and the spectral range is 10.5-12.5 μ M.

In the experiment, the common area of HJ-1B thermal infrared image and uf-2 image is intercepted. Aiming at the geometric correction of HJ-1B thermal infrared image, the traditional gray correlation, scale invariant feature transformation feature matching, gray correlation and SIFT feature matching of the simulated image are compared.

At present, the resolution of remote sensing thermal infrared image is generally low, and the resolution difference between thermal infrared image and optical image is objective. Therefore, this paper first reduces the spatial resolution difference between the two experimental images by downsampling, and then extracts the corresponding points by SIFT feature matching to realize the geometric correction of the image. At the same time, this method is compared with the classical method based on mutual information to analyze the effect of this method.

3.2 Thermal infrared image simulation

The information received by thermal infrared remote sensing sensor is the thermal radiation information of the earth's surface. The expression of radiation brightness value L_λ (radiation transfer equation) can be written as follows: (9)

$$L_\lambda = \left[\varepsilon B(T_S) + (1-\varepsilon)L^\uparrow\right]\tau + L^\downarrow \quad (9)$$

Where ε is the surface emissivity; T_S is the real surface temperature (k); $B(T_S)$ is the thermal radiance of blackbody; τ is the transmittance of the atmosphere in the thermal infrared band; $L^\uparrow$ is the upward radiance of the atmosphere; $L^\downarrow$ is the downward radiance of the atmosphere.

To simulate the image from the perspective of thermal infrared radiation transfer equation, it is necessary to determine the surface emissivity value ε, blackbody thermal radiance $B(T_S)$, atmospheric transmittance τ, atmospheric upward radiance $L^\uparrow$ and atmospheric downward radiance $L^\downarrow$.Through the website published by NASA, the atmospheric profile information can be obtained: atmospheric transmittance τ, atmospheric upward radiance $L^\uparrow$ and atmospheric downward radiance $L^\downarrow$.

For the estimation of specific emissivity ε, the vegetation index method, normalized vegetation index threshold method and NDVI threshold improvement method are widely used. In this experiment, the improved NDVI method is used to estimate the emissivity. Firstly, the normalized water index of the image is obtained. When NDWI > 0, it is divided into water body, otherwise it is divided into non water body. When the pixel is water body, ε = 0.995; when it is non water body, $\varepsilon = 0.004P_v + 0.986$; P_v is vegetation coverage. Table 1 shows the specific emissivity of some ground objects.

Table 1 Specific emissivity of ground objects

Features	Specific emissivity ε
Water body	0.995
Bare soil	0.986
Fully vegetated area	0.990
Vegetation partially covered area	0.986~0.990

The results show that there is a negative correlation between the real surface temperature A T_S and NDVI, and a negative correlation between the real water temperature T_w and NDWI. Therefore, we can roughly estimate the range of the surface temperature hole in the image range by looking up the meteorological data, establish the negative correlation between the hole and NDVI and NDWI, estimate the approximate surface temperature T_S according to the NDVI and

NDWI of the image, and then calculate the blackbody thermal radiation brightness $B(T_S)$ according to Planck formula. After all the above parameters are determined, the radiance of the thermal infrared image can be simulated according to the radiation transfer equation, and then the corresponding pixel brightness value can be calculated according to the radiometric calibration parameters provided by HJ-1B image, and the simulated image is formed after downsampling, as shown in Figure 5.

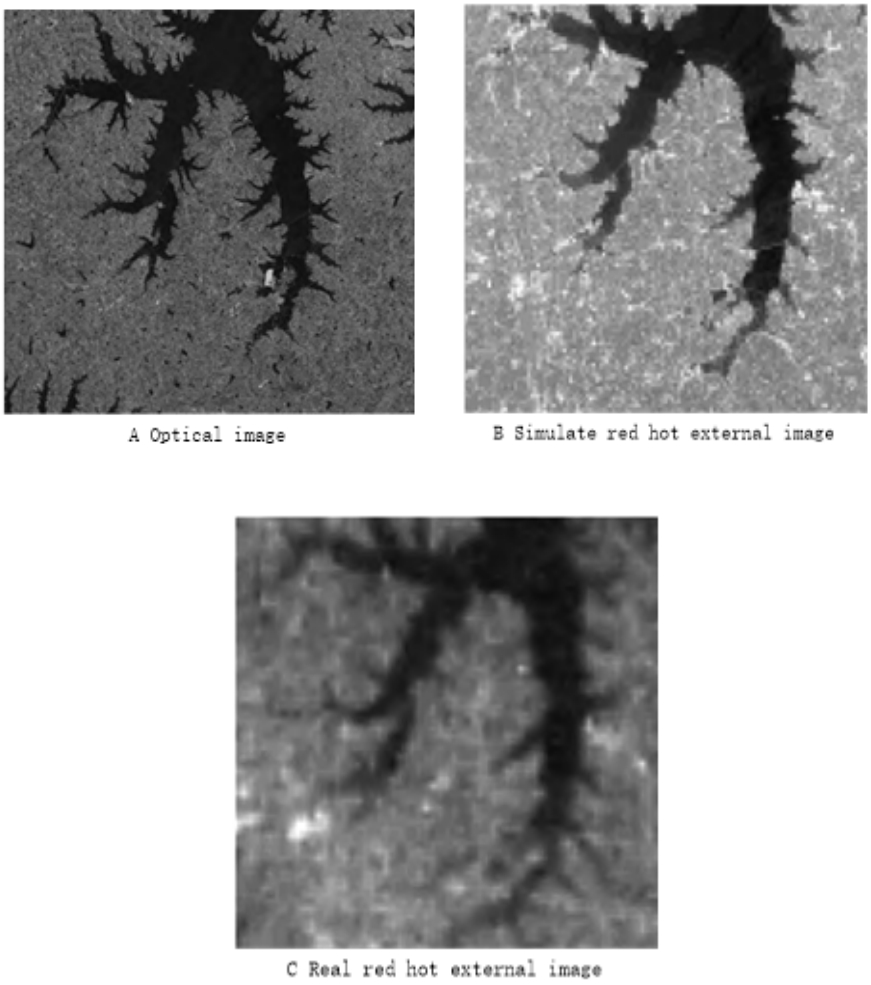

Fig. 5 Simulated image results

Considering the mechanism of radiation transmission, the gray level of simulated image and real image has good relative consistency through the relative relationship of ground radiance. Table 2 shows the detailed maps of different images

Table 2 Ground feature details of different images

Features	Optical image	Real thermal infrared image	Simulation image

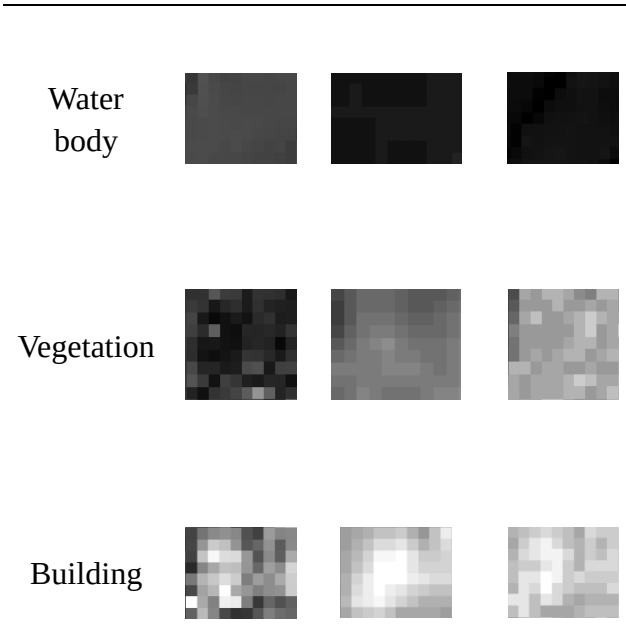

It can be seen from table 2 that the simulated image is closer to the real thermal infrared image in image characteristics than the optical image.

3.3 Simulation image matching

The infrared image features of each band were extracted based on the infrared image of sigf2 and HJ-1B. For the feature extraction of gray correlation, Harris operator is used to extract the feature points of gf-2 images and simulation images. The gray correlation is used as the measure, and the point with the largest correlation coefficient is found as its matching point on HJ-1B image. For SIFT feature extraction, the scale space extremum detection, extreme point precise location, key point main direction determination, key point description and other operations are used to obtain matching points with Euclidean distance as a measure.

There are still many false matching points between HJ-1B image and infrared image. In this paper, the random sampling consistency algorithm is used to eliminate the mismatched point pairs, and the remaining matching points are used to solve the geometric correction parameters of the right image, and the image point coordinates of the control points are calculated. According to the Euclidean distance between the image point coordinates and the matching point coordinates, the error difference value is calculated, and the points with the largest error are gradually eliminated until all the point pair errors are within one pixel As shown in Figure 6.

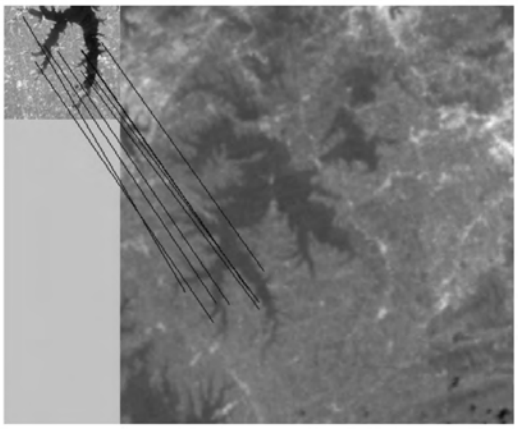

Fig. 6 Simulation image matching results

On the basis of the above matching points, the polynomial correction method can be used for geometric correction of the corrected image.

4 Results and analysis

Gf-2 image is a multispectral image, including data of four bands. For gray correlation and classic SIFT feature matching, the data of each band are matched with HJ-1B thermal infrared image respectively. The results are shown in Table 3.

Table 3 Data matching results of different methods and bands

Matching data	Gray correlation method		SIFT feature matching method	
	matching point	correct point	matching point	correct point
Gf-2 blue band	82	0	86	0
Gf-2 green band	90	0	85	0
Gf-2 red band	95	3	94	0
Gf-2 near infrared band	89	9	110	9
Simulation image	88	15	90	14

It can be seen from table 3 that for gf-2 images, only the red band and near-infrared band data have correct matching points in the gray correlation method, and there are no correct matching point pairs in the other bands, while the SIFT matching method only has the correct matching points for the near-infrared band data. This is because the infrared image reflects the radiation information of the ground object, while the image in the visible light band reflects the

reflection information of the ground object. The physical meaning of the surface feature information reflected by the two images is not the same. In addition, due to the different imaging conditions and the complexity of the ground objects, the correlation between the two images is small, so the gray characteristics of the two images are quite different, which makes it difficult to match. However, the gf-2 near infrared band and HJ-1B thermal infrared band images contain the radiation information of the ground objects, so there are some correct matching point pairs in the matching process the number of correct matching points is very small. After introducing the simulated image, the number of matching point pairs has increased to a certain extent. From the perspective of radiation transfer equation, the simulation image simulates the thermal radiation transmission process of ground objects, and the difference between the image formed and the HJ-1B thermal infrared image is significantly reduced. Although the simulation process takes approximate values for many parameters, it cannot truly represent the thermal redness of the actual ground objects However, simulation can reduce the difference between different images and improve the matching results. The above results also prove that the method proposed in this paper is feasible, which can improve the matching results between heterogeneous images and provide more matching points.

The HJ-1B thermal infrared image to be corrected is matched by SIFT features based on image simulation, and then corrected by polynomial method. The results are shown in Figure 7:

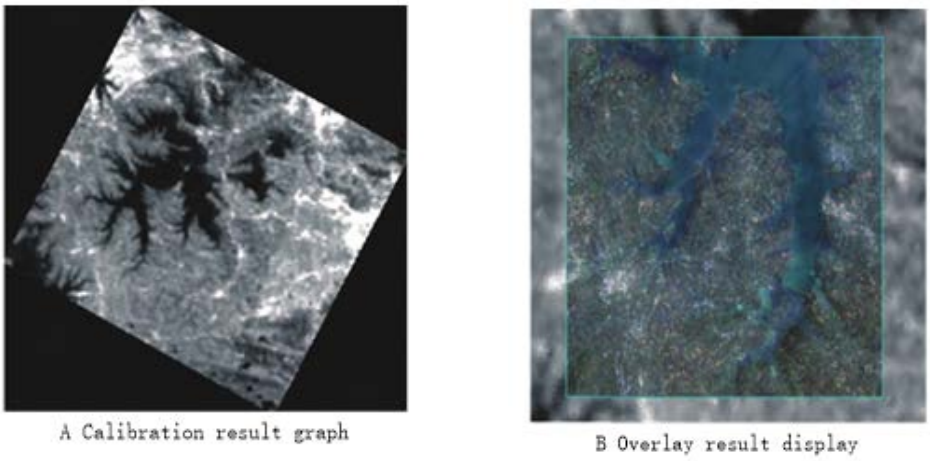

Fig. 7 HJ-1B image after correction

Table 4 lists the registration accuracy evaluation of some control points.

Table 4 Registration accuracy evaluation of control points

Serial number	Coordinate of matching point / image cable
1	(136.93,298.01)
2	(148.35,319.79)
3	(153.23,279.11)
4	(148.47,312.42)

5	(102.11,313.70)
6	(116.30,314.28)
7	(99.89，333.49)
8	(69.97,301.05)

It can be seen from table 4 that the maximum registration error of control points is 0.98 pixels, the minimum value is 0.35 pixels, and the average error is 0.60 pixels. The errors of the control points are all within 1 pixel, which meets the matching accuracy requirements. Through the remote sensing image processing platform, the corrected image is superimposed with the reference image, and the river and other features are observed. It is found that the corrected image can well match the reference image, and there is no obvious dislocation between the two, indicating that the correction result is good. This also proves that the method of geometric correction of thermal infrared image by image simulation is feasible.

Compared with the proposed method, the number of matching points obtained by the method based on mutual information is less, and the sub-pixel registration error effect obtained by this method is better. Therefore, compared with the traditional method, this method has more advantages in the accuracy and number of matching points.

References

[1] Weipeng J , Dongxue T , Guangsheng C , et al. Research on Improved Method of Storage and Query of Large-Scale Remote Sensing Images[J]. Journal of Database Management, 2018, 29(3):1-16.

[2] Xing Z , Li G . Intelligent Classification Method of Remote Sensing Image Based on Big Data in Spark Environment[J]. International Journal of Wireless Information Networks, 2019, 26(3):183-192.

[3] Fang, Chen, Jiang, et al. Research on Method of Farmland Obstacle Boundary Extraction in UAV Remote Sensing Images[J]. Sensors, 2019, 19(20):4431-.

[4] Cho K , Kim Y , Kim Y . Disaggregation of Landsat-8 Thermal Data Using Guided SWIR Imagery on the Scene of a Wildfire[J]. Remote Sensing, 2018, 10(2):105-.

[5] Yan Y , Zhang Y , Su N . A Novel Data Augmentation Method for Detection of Specific Aircraft in Remote Sensing RGB Images[J]. IEEE Access, 2019, PP(99):1-1.

[6] Ren C , Liang Y J , Lu X J , et al. Research on the soil moisture sliding estimation method using the LS-SVM based on multi-satellite fusion[J]. International journal of remote sensing, 2019, 40(5-6):2104-2119.

[7] Guo N , Zhan W . Research on the method of three-dimensional surface displacements of Tianjin area based on combined multi-source measurements[J]. Journal of Applied Geodesy, 2020, 14(1):83-94.

[8] Liu G , Li J . Research on the Effect of Tree Barriers on Rockfall Using a Three-Dimensional Discontinuous Deformation Analysis Method[J]. International Journal of Computational Methods, 2020, 17(08):455-471.

[9] Dai J , Wang Y , Li W , et al. Automatic Method for Extraction of Complex Road Intersection Points from High-resolution Remote Sensing Images Based on Fuzzy Inference[J]. IEEE Access, 2020, PP(99):1-1.

[10] Wang J F , Chen Z T , Hu X Y , et al. Research on method of high-precision 3D scene optical remote sensing imaging simulation[J]. Journal of Modern Optics, 2019, 66(3):1-12.